Center for Programmable Energy Catalysis

ChemRxiv™

Alumina-Titania Nanolaminate Condensers for Hot Programmable Catalysis

Kyung-Ryul Oh[1,2,†], Amber Walton[1,2,†], Jason Chalmers[1,3], Justin A. Hopkins[1,2], Jesse R. Canavan[1,2], Tzia Ming Onn[4], Susannah L. Scott[1,3], C. Daniel Frisbie[1,2], Paul J. Dauenhauer[1,2,*]

[1] Center for Programmable Energy Catalysis (CPEC), University of Minnesota, 421 Washington Ave. SE, Minneapolis, MN, USA 55455
[2] University of Minnesota, Department of Chemical Engineering & Materials Science, 421 Washington Ave. SE, Minneapolis, MN, USA 55455
[3] Department of Chemical Engineering, University of California Santa Barbara, 3357 Engineering II, Santa Barbara, CA, USA 93106
[4] Department of Engineering, University of Cambridge, Trumpington St., Cambridge CB2 1PZ, United Kingdom
† Authors contributed equally
*Corresponding author: hauer@umn.edu

Abstract. For programmable catalysis applications, nanolaminates composed of thin alternating layers of Al_2O_3 and TiO_2 (ATO) were engineered using atomic layer deposition (ALD) as the dielectric material for a Pt-on-carbon catalytic condenser. Systematic investigation assessed synthesis parameters such as deposition temperature, Al_2O_3 and TiO_2 layer thicknesses, the total number of layers (and interfaces), and the presence of a capping Al_2O_3 layer on the maximum achievable charge accumulation in the Pt catalyst layer. The highest capacitance ATO configuration demonstrated a specific capacitance of ~1,200 nF/cm^2 with working voltages of ±5 V, enabling the storage of 4×10^{13} electrons or holes per cm^2 at room temperature. Adsorption of carbon monoxide on the Pt/C-ATO device characterized by grazing incidence infrared spectroscopy showed changes in the surface binding energy of 13.1 ± 0.8 kJ/mol for an applied external voltage bias of ±1 V. The results enhance our understanding of nanolaminate structures and provide a method for increasing charge condensation strength for higher temperature surface chemistries.

1.0 Introduction. Catalytic condensers have active surfaces that can be tuned via the accumulation of a variable number of holes or electrons in an exposed catalyst layer, with the charge being stabilized across a dielectric film.[1,2] The goal is to apply a potential across the condenser architecture to modulate the electron density of catalytic sites with time, thereby enabling a 'programmable' sequence of surface electronic states that change on the time scale of a catalytic turnover.[3,4] Active condenser layers can consist of metal oxides, metals, or other surfaces with catalytic activity, making the condenser architecture amenable to most heterogeneous catalytic applications.

A challenge in condenser design is maximizing charge per active site under operating conditions relevant to catalytic chemistry. In previously reported condensers, a HfO_2 dielectric film about 70 nm thick permitted charge condensation in Pt/C or Al_2O_3/C of ~10^{13} |e$^-$| cm^{-2} and thermal stability (i.e., retains high capacitance and low capacitor leakage currents) up to 350 °C.[2,5,6] The extent of charge condensation was increased to ~10^{14} |e$^-$| cm^{-2} using a flexible ion gel film (in place of HfO_2) to achieve a higher overall device capacitance of ~2,000 nF/cm^2 at 25 °C, and ~20,000 nF/cm^2 at 200 °C.[7] However, the thermal stability of the ion gel composition (PVDF/ [EMIM]$^+$[TFSI]$^-$) allows functionality only up to 200 °C. This high temperature limit is below the targeted operability range (>200 °C) for many catalytic applications.

High-*k* dielectric films with high capacitance (>1,000 nF cm^{-2}) and thermal stability up to 400 °C would broaden the applicability of catalytic condensers to important reactions such as methanol and ammonia synthesis. Ferroelectric perovskite films such as lead titanate ($PbTiO_3$) and either strontium or barium titanate ($BaTiO_3$ or $SrTiO_3$)

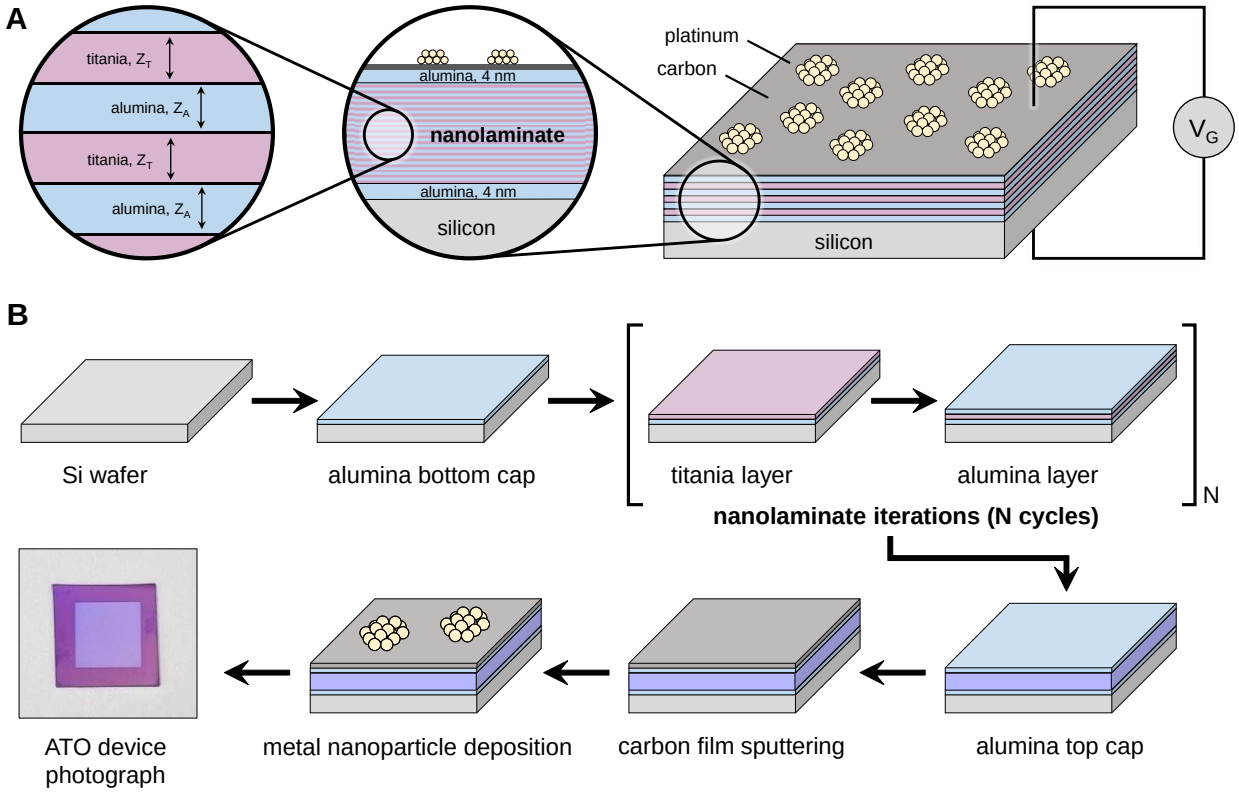

Figure 1. ATO Catalytic Condenser Design and Fabrication. (**A)** Schematic illustration of the alumina-titania (ATO) nanolaminate catalytic condenser. Z_C = thickness of the top and bottom capping Al_2O_3 layers. Z_A = thickness of the alternating Al_2O_3 sublayers. Z_T = thickness of the alternating TiO_2 sublayers. (**B)** ATO condensers are synthesized by atomic layer deposition with a thick bottom cap, followed by multiple alternating titania and alumina layers, followed by an alumina top cap. Carbon is then deposited on top to conduct charge, followed by metal nanoparticle catalyst. Bottom left: photograph of a 1 cm^2 Pt/C ATO catalytic condenser.

exhibit higher dielectric constants (k > 100) and greater stabilization of charge separation.[8,9] These perovskite-based films are traditionally fabricated via time- and cost-intensive deposition methods such as molecular beam epitaxy to ensure appropriate film crystallinity and stoichiometry. Alternatively, nanolaminate films consisting of alternating amorphous, sub-nanometer titania and alumina layers have been fabricated via atomic layer deposition or pulsed layer deposition, resulting in composite films with dielectric constants of 100 to 1,000,[10,11,12] that have been extensively evaluated.[13,14,15,16,17,18,19,20,21]

The high dielectric constants of alumina-titania nanolaminates (ATO) are attributed to the presence of oxygen vacancies in TiO_2 and charge accumulation at the interface of the alternating Al_2O_3 and TiO_2 layers due to their different conductivities, an effect known as Maxwell-Wagner relaxation.[10,11,12] This dielectric mechanism resembles the internal barrier layer capacitor structure in $CaCu_3Ti_4O_{12}$ ceramics, where the high capacitance arises from grain boundaries rather than the intrinsic properties of the material.[22,23] More broadly, nanolaminate structure comprised of alternating thin insulating layers (e.g., Al_2O_3 or HfO_2) and semiconducting layers (e.g., TiO_2 or ZnO) also exhibit high dielectric constants.[24,25,26,27] A systematic investigation of the influence of Al_2O_3 and TiO_2 layer thicknesses on the dielectric constant and leakage current (i.e., via tangent loss), Auciello and co-workers found that increasing the TiO_2 thickness or reducing the Al_2O_3 thickness while keeping the other sublayer thickness constant causes the dielectric constant as well as leakage current to increase.[13] They also reported that introducing a capping Al_2O_3 layer of 10 nm thickness lowered leakage current by several orders of magnitude, from 10^{-3} A/cm^2 to 10^{-9} A/cm^2,[12] albeit at the

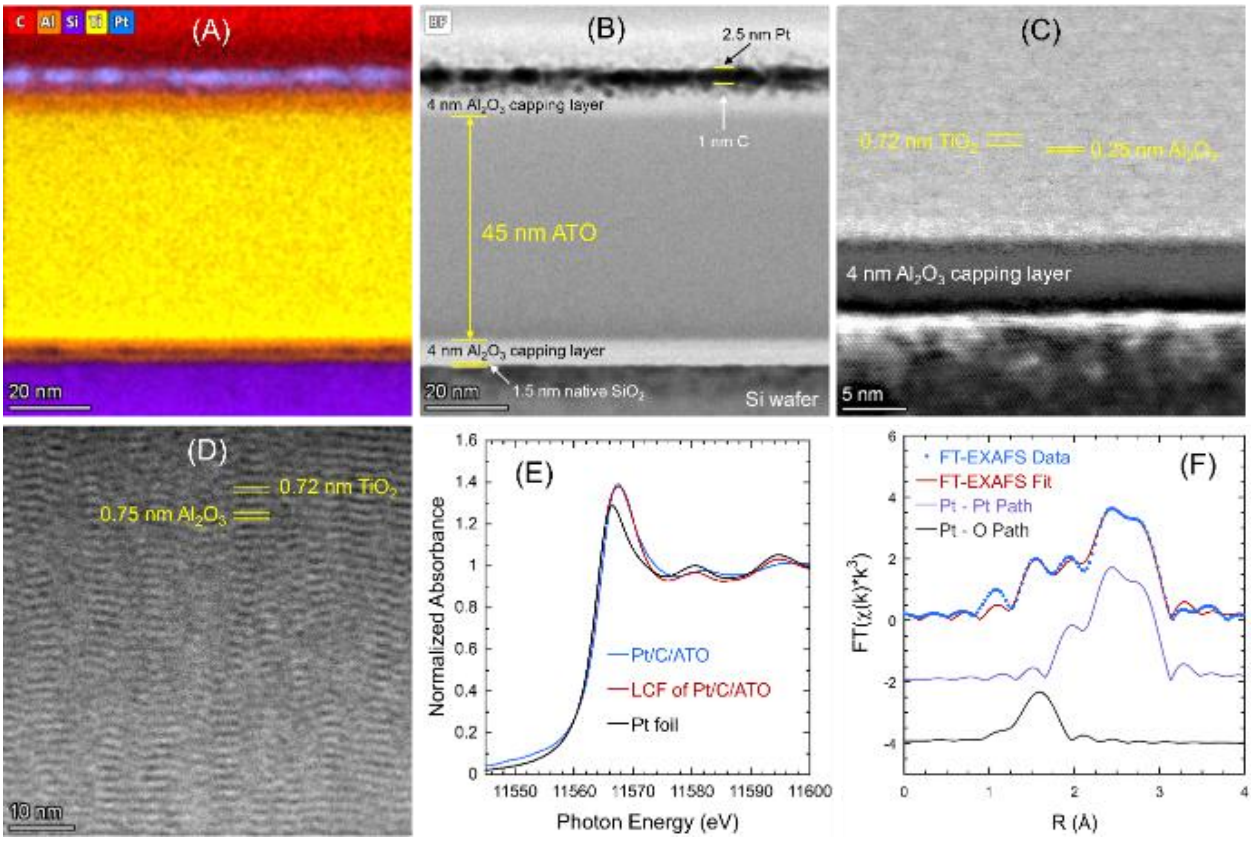

Figure 2. (A–C) Cross-section TEM images and EDS map of the ATO-3 catalytic condenser with Pt/C top layer and nanolaminate dielectric (0.25 nm alumina & 0.72 nm titania with 4 nm alumina capping layers) prepared at 300 °C. **(D)** Cross-section TEM image of ATO-10 catalytic condenser (0.25 nm alumina & 0.72 nm titania with 4 nm alumina capping layers) prepared at 300 °C. **(E)** Pt L_3-edge XANES with linear Combination Fit (LCF) for the Pt/C/ATO-5 condenser with a Pt foil reference spectra. **(F)** Data (points) and curvefit (lines) of the k^3 – weighted FT-EXAFS magnitude (top), the Pt – Pt contribution to the FT-EXAFS fit (middle) and the Pt – O contribution to the FT EXAFS fit (bottom) for the Pt/C/ATO-5 condenser, shown in nonphase-corrected R-space. Details are provided in the Supporting Information.

expense of the dielectric constant. The thermal stability of these nanolaminates and their maximum charge capacity, critical for their sustained operation as catalytic condensers at elevated temperatures (>200 °C) is important for their application. Moreover, the capacitive (dielectric) properties of nanolaminates at high temperatures (above 130 °C) have not previously been measured.[10,11,19]

Here, Pt/carbon condensers were fabricated from high dielectric nanolaminates composed of alternating thin (< 1 nm) layers of Al_2O_3 and TiO_2, designated 'ATO' (**Figure 1A)**. ATO films were prepared by atomic layer deposition (ALD) on a conductive, heavily doped *p*-type Si wafer, followed by carbon sputtering (1 nm) and e-beam deposition of Pt (2.5 nm), **Figure 1B.** A final Al_2O_3 capping layer (~4 nm) was deposited between the ATO dielectric film and both the top and bottom electrodes (Pt/C and p++-Si, respectively) to lower the leakage currents while maintaining high polarizability of the device stack. The capacitive currents and the thermal stabilities of the ATO materials were evaluated as a function of film thickness and growth temperature to identify design and fabrication methods leading to high capacitance and thermal stability.

Results and Discussion. *Fabrication and structural characterization of ATO-based catalytic condensers.* **Figure 1** shows a schematic of an ATO-based catalytic condenser. The design parameters include the thicknesses of the Al_2O_3 (Z_A/nm) and TiO_2 (Z_T/nm) sublayers, the thickness

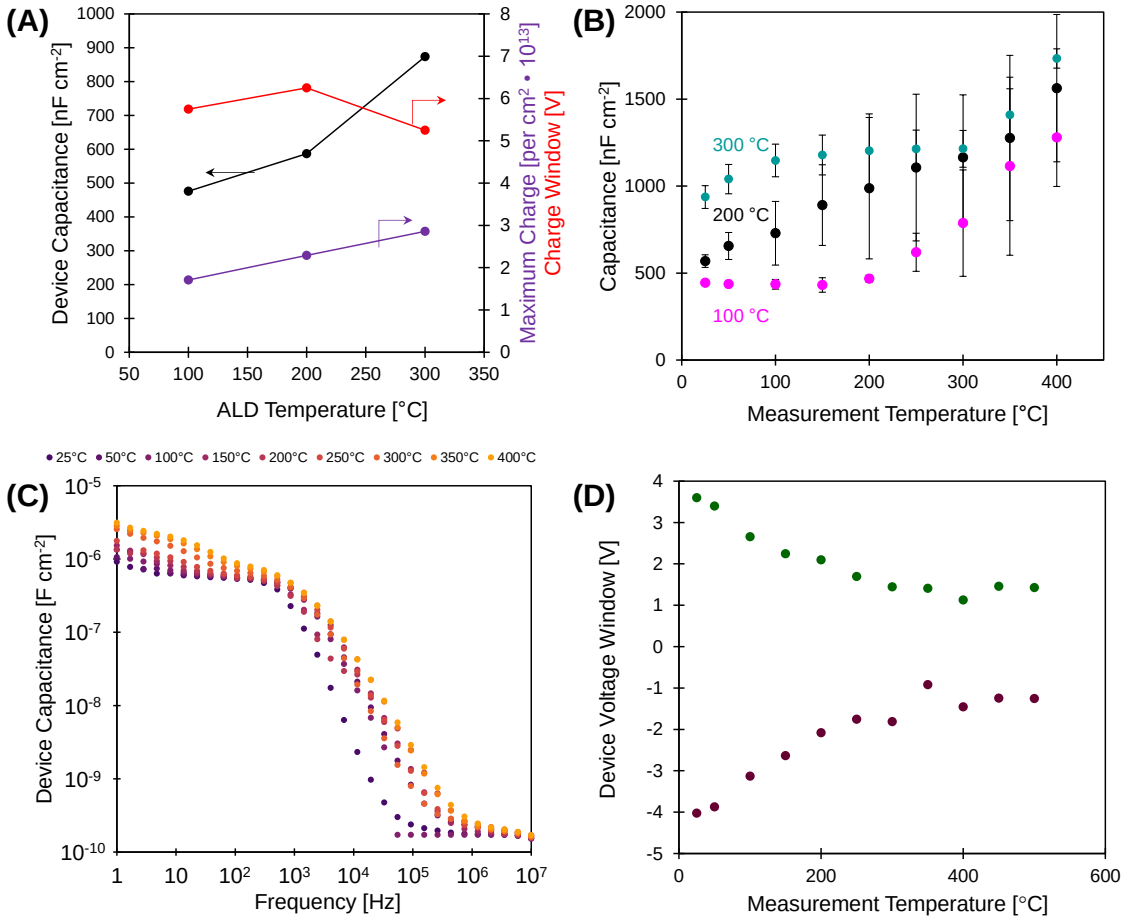

Figure 3. Electronic properties of ATO device with Pt/C top layer and nanolaminate dielectric (0.25-nm Al_2O_3 sublayer thicknesses and 0.72-nm TiO_2 sublayer thicknesses with 4-nm Al_2O_3 capping layers), prepared at different ALD deposition temperatures (ATO-1, ATO-2, ATO-3,see **Table S1**). **(A)** Comparison of capacitance, voltage window, and maximum charge (per cm^2) as a function of deposition temperature. **(B)** Comparison of capacitance as a function of measurement temperature for different deposition temperatures. **(C)** Comparison of impedance spectra for ATO-3 as a function of measurement temperature. **(D)** Comparison of voltage windows for ATO-3 as a function of measurement temperature.

of the Al_2O_3 capping layers (Z_C/nm), the number of interfaces (N) between alternating Al_2O_3 and TiO_2 sublayers, and the substrate temperature (T / °C) during ALD. **Table S1** summarizes the characteristics of each ATO device fabricated in this study. For each deposition temperature, sublayer growth rates determined using ellipsometry are presented in **Table S2**.

Cross-sectional transmission electron microscopy (TEM) analysis was conducted to confirm the thickness of each sublayer and to assess their uniformity. The energy dispersive spectroscopy (EDS) maps and TEM images of the ATO-3 device are shown in **Figure 2A-2D** and **Figure S1**, respectively. The device consists of a top Pt/C layer, the ATO nanolaminate (~45 nm), and Al_2O_3 capping layers (~4 nm) separating the ATO from the top Pt/C layer and from the bottom p-Si substrate (**Figure 2A**,**2B**). The ultra-thin alumina sublayers (0.25 nm) are difficult to distinguish from the titania sublayers (0.72 nm) by TEM due to the limited resolution (**Figure 2C**). To see the nanolaminate structure more clearly, ATO-10 was prepared with 0.75 nm alumina and 0.72 nm titania sublayers. The TEM analysis is shown in **Figure 2D**. The alumina and titania sublayers of the nanolaminate structure are visible. The observed uniformity and structural integrity of the ATO confirms the benefit of using ALD to fabricate high quality thin films, with discrete, alternating sublayers of alumina and titania. The electron diffraction (ED) patterns obtained from the ATO

stacks show that the Al_2O_3 and TiO_2 films are amorphous, as confirmed by X-ray diffraction (XRD) analysis (**Figure S2**), where the small-angle vertical streaking along the film growth direction confirms the nanolaminate structure (**Figure S3**)

The structure of the Pt layer in the catalytic condensers was investigated by X-ray absorption spectroscopy (XAS), as shown in **Figure 2E** & **2F**. The Pt L_3-edge edge, 11,564.8 eV, and the whiteline maximum, 11,567.5 eV from X-ray absorption near edge spectroscopy (XANES) data (**Figure 2E, Figure S4**), indicate that Pt is partially oxidized at the surface. A linear combination fit showed that (89 ± 1)% of Pt is metallic, while (11 ± 1)% is Pt (IV). Recent studies have confirmed the growth of disordered surface platinum oxides on Pt (111) surfaces at ~300 K and 0.001–1 bar O_2,[28,29] therefore, this result is reasonable considering the Pt/carbon catalytic condenser was exposed to air prior to the XAS measurements. The average Pt particle size estimated by fitting the extended X-ray absorption fine structure (EXAFS) gave an average Pt–Pt coordination number of (5.9 ± 0.4), with a bond distance of (2.71 ± 0.01) Å (**Figure 2F, Figure S5, Table S3**). These values are consistent with 1.5–2 nm Pt nanoparticles.[30] No longer range Pt–Pt paths were observed in the EXAFS, indicating that the nanoparticles are small and disordered. Considering only ~10 % of the Pt is oxidized but 1.5–2 nm Pt nanoparticles have a Pt dispersion of 50–70 %,[31] this suggests only a fraction of the Pt surface was oxidized.

Electronic properties of ATO-based catalytic condensers. The capacitance and operational voltages of the ATO-based devices were characterized by I–V (DC) measurements (**Figure S6–S14**) and impedance spectroscopy. The dielectric constant or capacitance of a nanolaminate ATO film is correlated with the number of oxygen defects (vacancies) in the TiO_2 layer.[10] Modifying the ALD growth temperature influences the defect density, providing a method to tune ATO capacitance.[32] **Figure 3A** compares the room temperature electronic properties of ATO-based devices fabricated at 100, 200, and 300 °C, all other parameters being constant (Z_A = 0.25 nm, Z_T = 0.72 nm, Z_C = 4 nm, N = 91). The resulting capacitances were 476, 587, and 874 nF/cm^2, respectively (**Figure 3A**, black ●), indicating that higher growth temperatures result in higher capacitance.

To investigate whether the increase in capacitance is due to a higher number of defects (oxygen vacancies) in the TiO_2 layer, 5 nm TiO_2 layers were grown at 100, 200, and 300 °C and analyzed by X-ray photoelectron spectroscopy (XPS), **Figure S15**. The presence of an unsymmetrical peak in the O 1*s* region (**Figure S15a**) indicates oxygen atoms in various chemical states. Metal oxide films grown via ALD include not only lattice oxygen but also oxygen vacancies and surface impurities (-OH groups).[33,34,35] Consequently, the O 1*s* region was deconvoluted into three components: O_L (lattice oxygen), O_D (defective oxygen bound to Ti^{3+}), and O_{OH} (surface hydroxyl). Table S4 shows that the surface hydroxyl concentration has a relative 10% decrease (from 8.8% to 7.9%) as the deposition temperature increases. In contrast, the oxygen vacancy concentrations nearly double with deposition temperature, from 7.2% to 15.1%. The Ti 2*p* region shows the expected Ti $2p_{3/2}$ and Ti $2p_{1/2}$ peaks (**Figure S15b**). Despite the complexity of their deconvolution, the binding energies for both peaks do shift slightly to higher energies as the deposition temperature increases. Since the binding energies for Ti^{3+} are lower ($2p_{3/2}$: 458.07 eV, $2p_{1/2}$: 463.70 eV) than for Ti^{4+} ($2i_{3/2}$: 459.39 eV, $2p_{1/2}$: 465.17 eV),[21] the shift suggests a higher concentration of Ti^{3+} and corresponding oxygen vacancies when deposition is conducted at higher temperatures. Therefore, the XPS result is consistent with the larger capacitance at higher deposition temperatures, due to a higher defect concentration in the TiO_2 sublayers. XRD analysis of ATO films grown at the same temperatures confirms that the films remain amorphous under all deposition conditions, eliminating the possibility that crystallization is responsible for the observed changes in capacitance (**Figure S2)**.

The operable voltage window also determines the total charge accumulation ($Q = C \times V$, where Q = charge amount, C = capacitance, V = voltage) in a catalytic condenser. The voltage windows were defined at the intersection of lines extrapolated from the low and high voltage bias regimes of the current versus voltage scans at 1 V/s. The voltage windows of ATO devices prepared at 100, 200, and 300 °C were similar (±5.75, ±6.25, and ±5.25 V, **Figure 3A**, red). The capacitance and voltage window were used to calculate the maximum charge accumulation (e^- or h^+), **Figure 3A** (purple).

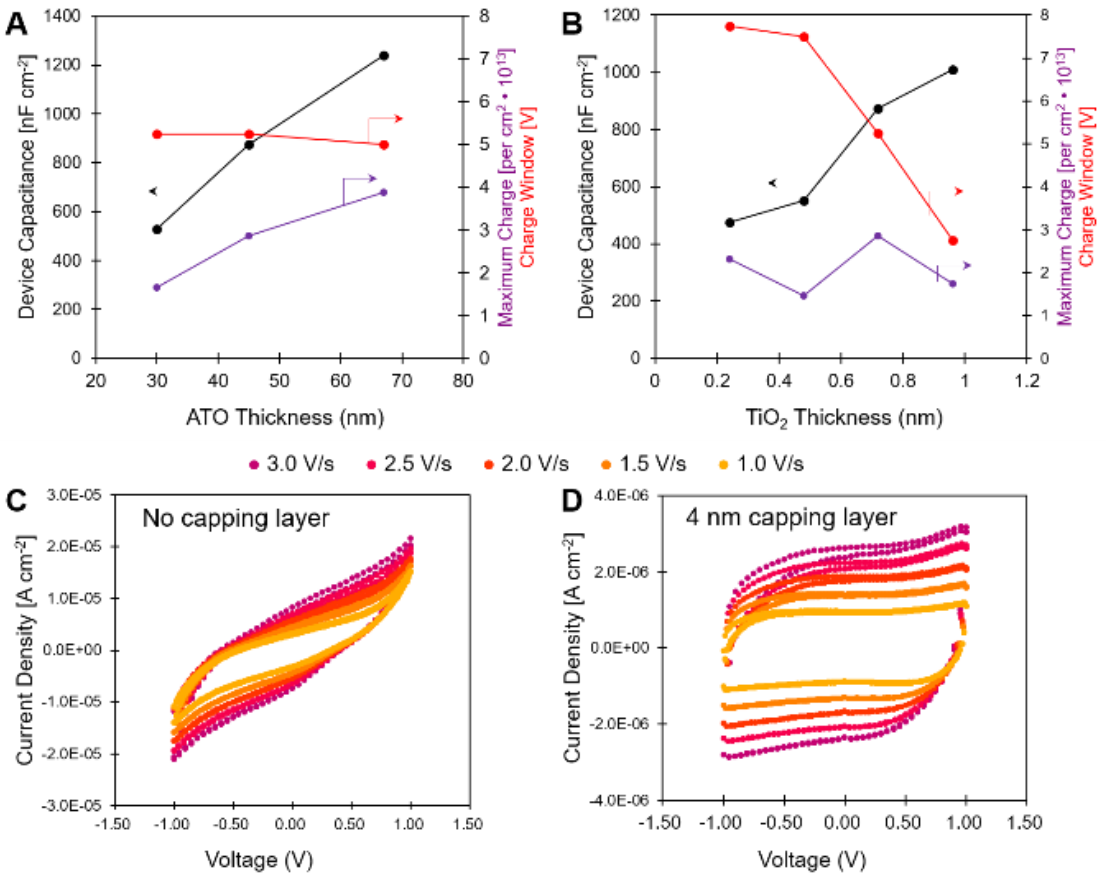

Figure 4. Variation in Nanolaminate Structural Parameters. **(A)** Comparison of device capacitance with total nanolaminate thickness varied by changing the number of 0.25-nm Al_2O_3 sublayers and 0.72-nm TiO_2 sublayers (all with 4-nm Al_2O_3 capping layers). **(B)** Comparison of device capacitance with the TiO_2 sublayer thickness. **(C-D)** Comparison of current densities with and without Al_2O_3 capping layers (4-nm thickness).

The device made at 300 °C had the highest charge density (2.9×10^{13}/cm^2) at room temperature.

To characterize changes in electronic properties of the devices at elevated temperatures, I–V measurements were conducted while the device was heated in air on a hot plate, **Figure 3B**. At each temperature setpoint, the device was allowed to thermally equilibrate for three minutes prior to measurement. The devices grown at different temperatures exhibited distinct capacitances. As the measurement temperature increased from room temperature to 400 °C, the capacitance increased significantly (for ATO-1: from 444 to 1280 nF/cm^2; for ATO-2: from 569 to 1560 nF/cm^2; for ATO-3: from 937 to 1733 nF/cm^2). This temperature trend is attributed to higher rates of diffusion of oxygen vacancies towards the Al_2O_3-TiO_2 interface due to the promotion of molecular motion of charge carriers at elevated temperatures, resulting in the increased dielectric constant.[19]

Since ATO-3 showed the highest capacitance and largest charge modulation ability across the evaluated temperature range (25–400 °C), the electronic properties of ATO-3 were analyzed further. **Figure 3C** shows impedance spectra of ATO-3 at different temperatures (from 25 to 400 °C). The capacitance increases significantly with temperature (from 920 to 3120 nF/cm^2), consistent with the I–V measurements. As the frequency increased from 1 to 1,000 Hz, the device capacitance decreased slightly; at higher frequencies, the capacitance declined rapidly due to the limited conductance of the Pt/C layer, as reported previously.[6] The operable voltage window of ATO-3 was measured at various temperatures, **Figure 3D**. The magnitude of the achievable voltage decreased in both the positive and negative directions as a function of temperature, indicating that a significant increase in the leakage current reduces the voltage range

despite the higher device capacitance at elevated temperatures.

The capacitance of dielectric films consisting of a single metal oxide (*e.g.*, HfO_2) is inversely proportional to film thickness.[36] However, ATO nanolaminate films behave differently; the total device capacitance *increases* with total nanolaminate film thickness (i.e., entire ATO) and the total number of sublayers. **Figure 4A** compares the capacitances and working voltages of ATO condensers with different numbers of interfaces, all other parameters being constant (Z_A = 0.25 nm, Z_T = 0.72 nm, Z_C = 4 nm, T = 300 °C). Notably, the capacitance increases linearly (from 530, to 874, and to 1243 nF/cm^2) with ATO thickness. This result indicates that the capacitance of ATO nanolaminates is due to charge accumulation at the Al_2O_3-TiO_2 interfaces. Since all three devices exhibit similar voltage windows (5.0 to 5.3 V), the maximum charge amounts also increase (from 1.6×10^{13}/cm^2 to 3.9×10^{13}/cm^2) with the number of interfaces (from 61 to 137 layers). **Figure 4B** compares the electronic properties of ATO as a function of TiO_2 sublayer thickness, while keeping the Al_2O_3 sublayer thickness constant (Z_A = 0.25 nm). The capacitance increases with TiO_2 thickness independent of the number of interfaces. This result is attributed to the higher number of defects in thicker TiO_2 sublayers. However, the applied voltage window decreases with increased TiO_2 sublayer thickness, indicating a trade-off between capacitance and voltage window. The optimum TiO_2 sublayer thickness to achieve high capacitance as well as a large voltage window is 0.72 nm.

The importance of the Al_2O_3 capping layer between the ATO and the electrodes was evaluated. Current-voltage curves for ATO devices are compared with and without 4 nm capping layers are compared in **Figure 4C** & **4D**. ATO without capping layers exhibits a high capacitance (1920 nF/cm^2), but also a high leakage current (~10^{-5} A/cm^2 at 1 V). In contrast, the ATO device with 4 nm Al_2O_3 capping layers gave box-shaped current-voltage curves with a significantly lower leakage current (~10× lower). Furthermore, the voltage window increases from 1.9 to 5.3 V when 4 nm Al_2O_3 capping layers are present, resulting in increased total condensed charge. Thus, capping layers are important for maximizing the total charge in catalyst active sites in device applications based on ATO nanolaminates.

IR of CO adsorbed on Pt/C ATO condensers. The behavior of CO chemisorbed on metal sites in catalytic condensers as a function of applied voltage bias provides evidence for charging of the active sites.[5,6,7] **Figure 5A** (inset) shows isobaric adsorbed CO infrared spectra for the ATO-5 device (maximum charge = 3.9×10^{13}/cm^2 at room temperature) measured at different temperatures while varying the applied potential bias (−1, 0 , +1 V). (Complete IR spectra are provided in **Figure S16**.) Peaks for CO(g) (2123 and 2180 cm^{-1}) and adsorbed CO* (2057 cm^{-1}) are visible. As the reactor temperature increases, the peak area for Pt-CO decreases as the surface coverage CO* decreases. **Figure 5A** shows the CO* coverage normalized to the highest area peak at low temperature (25 °C) as a function of temperature for different voltage biases. At 0 V, 50 % coverage of CO* occurs at 115 °C. At −1 V, 50% coverage occurs at a lower temperature (85 °C), while a higher temperature (135 °C) is required at +1 V to achieve 50% coverage of CO*. The variation in coverage with applied voltage is consistent with our previous results, where applying a negative potential cause electrons to condense at the Pt surface, weakening the metal-CO bond, and reducing the CO desorption temperature.[5,6,7] In contrast, applying a positive potential (+1 V) results in a higher temperature for CO desorption due to the increased Pt-CO bond strength.

Using the normalized CO coverages, Langmuir adsorption isobars were fitted (**Figure 5A**, solid lines). The heat of CO adsorption was estimated at each potential bias, **Figure 5B** (details of the adsorption model are provided in the Supporting Information). The difference in CO binding energies at −1 and +1 V, 13.1 ± 0.8 kJ/mol, indicates a shift in the binding energy of 6.5 kJ/mol per applied volt. HfO_2-based and ion gel devices, having capacitances of 340 and 2400 nF/cm^2, respectively. Showed shifts in CO binding energies of 1.5 and 14.6 kJ/mol per applied volt, **Figure 5C**.[5,7] Although the thermal behavior of the electronic properties (capacitance, leakage current) of these three devices differ, the shift in binding energy per applied volt is a linear function of device capacitance at room temperature.

The high capacitance (~1200 nF/cm^2) and substantial charge density (~4 ×10^{13}/cm^2) of the ATO-based catalytic condensers suggest that nanolaminates can be useful dielectric materials for

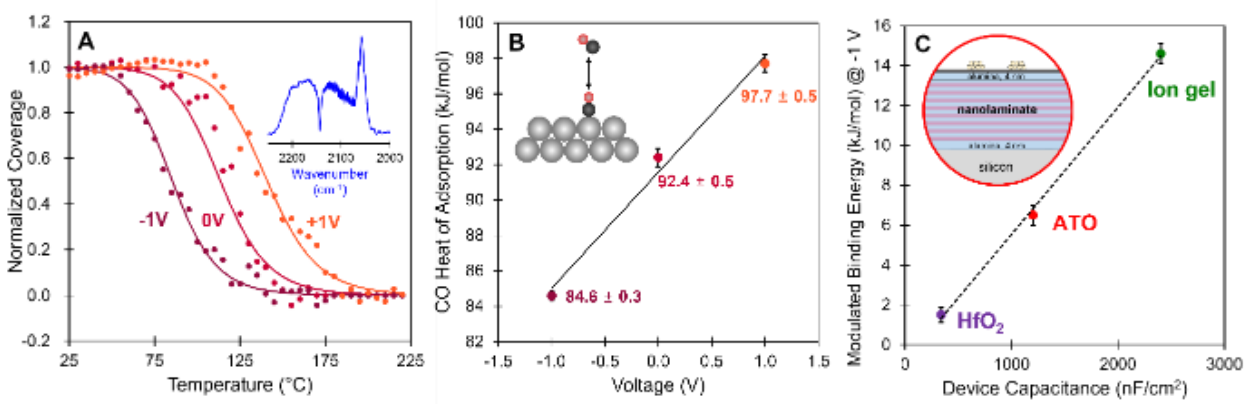

Figure 5. Grazing Incidence IR Spectroscopy of CO Adsorbed on a Pt/C ATO condenser. **(A)** Normalized CO coverage on the Pt/C ATO-5 catalytic condenser as a function of temperature at three voltage biases (−1 V, 0 V, and +1 V). Points: experimental data, lines: fitted Langmuir isobars. **(B)** Binding energies of CO on Pt obtained from the Langmuir isobars at each potential bias. **(C)** Comparison of CO binding energies on Pt in condensers with HfO_2, ATO, and ion gel dielectric films, all measured with an applied potential of −1 V.

catalytic applications. Their thermal stability (up to ~500 °C) may make them suitable for high temperature catalytic applications, such as methanol decomposition, CO oxidation, and ammonia synthesis and decomposition.[37] Programmable catalysis achieved by dynamic modulation of surface charge density is predicted to achieve faster catalytic rates with larger variations in charge condensation.[38,39,40] The alternation of insulating and semiconducting layers in nanolaminates imparts high capacitance (2 μF/cm^2) with the capability for fast response (1,000 Hz). Further investigations to enhance and optimize these characteristics for faster and more powerful condenser devices are underway.

Conclusion. Alumina-titania nanolaminate (ATO) films were synthesized as the dielectric material of Pt-on-carbon catalytic condensers. Their electronic properties and thermal stability were characterized to determine the extent of charge accumulation in the Pt active layer. TEM analysis confirmed the uniformity and desired thickness of the thin Al_2O_3 and TiO_2 sublayers. A higher ALD deposition temperature (300 °C) caused the number of oxygen vacancies in the TiO_2 sublayers to increase, resulting in higher capacitance compared to devices prepared at lower temperatures (100 or 200 °C). The addition of Al_2O_3 capping layers (4 nm) reduces device capacitance but enhances the maximum charge condensed due to the expanded voltage window across which the current leakage is minimal. Increasing the number of interfaces (i.e., adding ATO sublayers) results in increased capacitance, consistent with dielectric properties that originate from the alumina-titania interface. Infrared spectra of CO adsorbed on Pt in devices with ATO as the dielectric demonstrates that charge modulation shifts the CO binding energy. Due to its high capacitance (~1200 nF/cm^2) and robust thermal stability, ATO-based catalytic condensers may be viable for controlling catalytic chemistry at temperatures above 200 °C.

Experimental Methods. *Fabrication of ATO nanolaminates by atomic layer deposition (ALD).* A highly conductive *p*-type Si wafer (Waferpro, Item # C04005, P/B <1-0-0>, with resistivity ≤ 0.005 Ohm-cm), was used as a substrate. The substrate was rinsed three times with acetone and 2-propanol, then dried with a N_2 gun before use. The TMA (trimethylaluminum) and TDMAT (*tetrakis*(dimethylamido)titanium(IV)) were used as the precursors for Al_2O_3 and TiO_2, and water was used as the hydrolyzing agent. The growth rates of Al_2O_3 and TiO_2 at various temperatures (100, 200, 300 °C) were determined by measuring the thickness of films after 100 cycles, using an ellipsometer (Film Sense LLC). The ATO nanolaminate was fabricated by alternating the growth of desired thicknesses of Al_2O_3 and TiO_2. To reduce the leakage current, two additional Al_2O_3 capping layers (2–4 nm) was grown between both:

(i) the ATO and top (Pt/C), and (ii) between the ATO and bottom (p+++-Si) electrodes.

Carbon Sputtering. A carbon film was deposited on top of the ATO film using a sputter coater (Leica EM ACE600). Carbon thread was used as the carbon source, and the sputtering was performed at 140 W under vacuum (5.0×10^{-5} Torr) until 1 nm of carbon film deposition was measured by the quartz crystal microbalance in the sputtering machine.

E-beam Evaporation of Pt. A Pt layer was grown by electron-beam evaporation (CHA evaporator), using a Pt target source. The deposition proceeded at 1 Å/s until the film reached the desired thickness of 1 nm, as measured by quartz crystal microbalance.

X-ray Absorption Spectroscopy (XAS). XAS step-scan measurements were recorded at the Pt L_3-edge (10,564.0 eV) on beamline 11-2 of the Stanford Synchrotron Radiation Lightsource (SSRL), which operates at 3.0 GeV and a current of 500 mA. A liquid N_2-cooled Si(220) monochromator at f = 0° was used to select the X-ray energy, with a Rh-coated collimating mirror for harmonic rejection. The X-ray energy was calibrated by setting the maximum in the first derivative of Pt foil to 11,564.0 eV. Pt/C/ATO condensers were first exposed to air, and then placed in a He-filled custom sample cell located after the first ionization chamber. Samples were mounted on a rotating stage to allow for grazing incidence XAS measurements. The Pt Lα1 fluorescence line intensity was monitored with a 100-element Ge detector, perpendicular to the X-ray beam. XAS data processing and analysis were performed using the Demeter software package.[41] In a linear combination fitting, Pt foil and $Na_2Pt(OH)_6$ spectra were used as references for Pt(0) and Pt(IV) sites (**Figure S4**), respectively.

Electronic Measurements. Prior to measurement, a small portion of the bottom of the sample was gently scratched with a scribe to remove the native oxide from the silicon wafer. Electrical contact was made to the device via tungsten probes, where topside contact was made directly to the Pt/C layer and the bottom side was grounded via probe contact to the conductive stage underneath the sample. The electronic measurements were conducted using a probe station equipped with a source meter (Keithley 2612B and Keithley Test Script Builder). Topside voltages were scanned between ±1 V at different voltage sweep rates (1.00 – 3.00 V/s) to determine the device capacitance at 0 V. The voltage window was gradually increased to observe leakage behavior and determine the maximum operable potential. Impedance spectra were collected using a multimeter (Newtons PSM3750) equipped with an Impedance Analysis Interface 2, with a frequency range from 1 Hz to 10 MHz. For high temperature measurements, the device was placed on a conductive stainless-steel piece for bottom contact on top of a ceramic hot plate.

Device characterization. XPS characterization was performed using a PHI 5000 VersaProbe III Photoelectron Spectrometer. Peak fitting was conducted using mixed Gaussian-Lorentzian functions superimposed on an integrated Shirley background. The largest intensity C 1*s* peak was assigned an energy of 284.8 eV for each scan to correct for charging. XRD characterization was performed using a Bruker D8 Discover with Co Kα radiation (λ = 0.179 nm) and an areal detector. The cross sections of the devices for TEM studies were prepared using a focused ion beam (FEI Helios NanoLab G4 Dual Beam). Approximately 50 nm of protective amorphous carbon was deposited prior to the preparation of lamellar cross sections using a Ga ion beam operated at energies of 30, 5, 2, and 1 keV. HRTEM, STEM, and EDS characterizations were performed using a Thermo Fisher Talos F200X G2 microscope equipped with a Super-X EDS spectrometer and Thermo Fisher Velox software. The microscope was operated by using an electron beam energy of 200 keV.

CO isobar IR study. The CO isobar IR study was conducted using a Thermo Scientific Nicolet iS50 FTIR spectrometer equipped with a deuterated triglycine sulfate (DTGS) detector, wedged ZnSe windows, and a modified RefractorReactor™ grazing incidence angle accessory (Harrick Scientific, RGR-XXX-3).[5] The incident angle of the beam was fixed at 75°. The IR cell was equipped with electrical feedthroughs connected to a sourcemeter (Keithley 2450). An ATO device with top Pt/C surface was placed in an IR cell, and electrical contact was made using stainless steel wires. Before each CO isobar experiment, current-voltage measurements were conducted to establish the device capacitance (~1200 nF/cm^2) using a sourcemeter. After sealing, the IR cell was evacuated to a base pressure of 100 mTorr before

collecting a background spectrum. Next, 7.6 Torr CO was introduced into the cell at room temperature, and the CO(g) pressure was maintained for equilibrium between gaseous CO(g) and surface-adsorbed CO*. Then, the reactor temperature was incrementally raised by 5 °C intervals (ramp rate of 20 °C/min), and CO isobar IR data were collected at each 5 °C increment following a one-minute hold period, while applying a potential bias (−1 V, 0 V, +1 V). The schematic of the IR setup and the details of the Langmuir modeling method can be found elsewhere.[5,7]

Acknowledgements. This work was supported as part of the Center for Programmable Energy Catalysis, an Energy Frontier Research Center funded by the U.S. Department of Energy, Office of Science, Basic Energy Sciences at the University of Minnesota under award #DE-SC0023464.

Supporting information. The Supporting Information is available free of charge.

Keywords. Catalyst, Condenser, Laminate, Titania, Alumina

References

(1) Shetty, M.; Walton, A.; Gathmann, S. R.; Ardagh, M. A.; Gopeesingh, J.; Resasco, J.; Birol, T.; Zhang, Q.; Tsapatsis, M.; Vlachos, D. G.; Christopher, P.; Frisbie, C. D.; Abdelrahman, O. A.; Dauenhauer, P. J. The Catalytic Mechanics of Dynamic Surfaces: Stimulating Methods for Promoting Catalytic Resonance. *ACS Catalysis* **2020**, 12666–12695. https://doi.org/10.1021/acscatal.0c03336.

(2) Onn, T. M.; Gathmann, S. R.; Wang, Y.; Patel, R.; Guo, S.; Chen, H.; Soeherman, J. K.; Christopher, P.; Rojas, G.; Mkhoyan, K. A.; Neurock, M.; Abdelrahman, O. A.; Frisbie, C. D.; Dauenhauer, P. J. Alumina Graphene Catalytic Condenser for Programmable Solid Acids. *JACS Au* **2022**. https://doi.org/10.1021/jacsau.2c00114.

(3) Dauenhauer, P. J. Up Up Down Down Left Right Left Right B A Start for the Catalytic Hackers of Programmable Materials. *Matter* **2023**. https://doi.org/10.1016/j.matt.2023.11.008.

(4) Ardagh, M. A.; Abdelrahman, O. A.; Dauenhauer, P. J. Principles of Dynamic Heterogeneous Catalysis: Surface Resonance and Turnover Frequency Response. *ACS Catalysis* **2019**, *9* (8), 6929–6937. https://doi.org/10.1021/acscatal.9b01606.

(5) Onn, T. M.; Gathmann, S. R.; Guo, S.; Solanki, S. P. S.; Walton, A.; Page, B. J.; Rojas, G.; Neurock, M.; Grabow, L. C.; Mkhoyan, K. A.; Abdelrahman, O. A.; Frisbie, C. D.; Dauenhauer, P. J. Platinum Graphene Catalytic Condenser for Millisecond Programmable Metal Surfaces. *Journal of the American Chemical Society* **2022**, *144* (48), 22113–22127. https://doi.org/10.1021/jacs.2c09481.

(6) Oh, K.-R.; Onn, T. M.; Walton, A.; Odlyzko, M. L.; Frisbie, C. D.; Dauenhauer, P. J. Fabrication of Large Area Metal-on-Carbon Catalytic Condensers for Programmable Catalysis. *ACS Applied Materials & InterfacesMaterials* **2023**. https://doi.org/10.1021/acsami.3c14623.

(7) Onn, T. M.; Oh, K.-R.; Adrahtas, D. Z.; Soeherman, J. K.; Hopkins, J. A.; Frisbie, C. D.; Dauenhauer, P. J. Flexible and Extensive Platinum Ion Gel Condensers for Programmable Catalysis. *ACS Nano* **2023**. https://doi.org/10.1021/acsnano.3c09815.

(8) Nunn, W.; Kumar, A.; Zu, R.; Nebgen, B.; Yu, S.; Kamath Manjeshwar, A.; Gopalan, V.; LeBeau, J. M.; James, R. D.; Jalan, B. Sn-Modified BaTiO3 Thin Film with Enhanced Polarization. *Journal of Vacuum Science & Technology A* **2023**, *41* (2), 22701. https://doi.org/10.1116/6.0002208.

(9) Jung, S.; Pizzolitto, C.; Biasi, P.; Dauenhauer, P. J.; Birol, T. Programmable Catalysis by Support Polarization: Elucidating and Breaking Scaling Relations. *Nature Communications* **2023**, *14* (1), 7795. https://doi.org/10.1038/s41467-023-43641-0.

(10) Li, W.; Auciello, O.; Premnath, R. N.; Kabius, B. Giant Dielectric Constant Dominated by Maxwell-Wagner Relaxation in Al2O3 / TiO2 Nanolaminates Synthesized by Atomic Layer Deposition. *Applied Physics Letters* **2010**, *96* (16). https://doi.org/10.1063/1.3413961.

(11) Li, W.; Chen, Z.; Premnath, R. N.; Kabius, B.; Auciello, O. Controllable Giant Dielectric Constant in AlOx/TiOy Nanolaminates. *Journal of Applied Physics* **2011**, *110* (2). https://doi.org/10.1063/1.3603002.

(12) Lee, G.; Lai, B. K.; Phatak, C.; Katiyar, R. S.; Auciello, O. Interface-Controlled High Dielectric Constant Al2O3/TiOx Nanolaminates with Low Loss and Low Leakage Current Density for New Generation Nanodevices. *Journal of Applied Physics* **2013**, *114* (2). https://doi.org/10.1063/1.4811810.

(13) Lee, G.; Lai, B. K.; Phatak, C.; Katiyar, R. S.; Auciello, O. Tailoring Dielectric Relaxation in Ultra-Thin High-Dielectric Constant Nanolaminates for Nanoelectronics. *Applied Physics Letters* **2013**, *102* (14).

https://doi.org/10.1063/1.4790838.

(14) Lee, G.; Katiyar, R. S.; Lai, B. K.; Phatak, C.; Auciello, O. Dielectric Behavior Related to TiOx Phase Change to TiO2 in TiOx/Al2O3 Nanolaminate Thin Films. *MRS Communications* **2014**, *4* (2), 67–72. https://doi.org/10.1557/mrc.2014.14.

(15) Auciello, O.; Lee, G.; Wu, C.; Chen, Y.; Alcantar-Peña, J. J.; Mejia, I.; De Obaldía, E. Super High-Dielectric-Constant Oxide Films for next-Generation Nanoelectronics and Supercapacitors for Energy Storage. *MRS Bulletin* **2020**, *45* (3), 231–238. https://doi.org/10.1557/mrs.2020.67.

(16) Liu, J.; Auciello, O.; de Obaldia, E.; Da, B.; Koide, Y. Science and Technology of Integrated Super-High Dielectric Constant AlOx/TiOy Nanolaminates / Diamond for MOS Capacitors and MOSFETs. *Carbon* **2021**, *172*, 112–121. https://doi.org/10.1016/j.carbon.2020.10.031.

(17) Walke, P.; Bouregba, R.; Lefevre, A.; Parat, G.; Lallemand, F.; Voiron, F.; Mercey, B.; Lüders, U. Giant Dielectric Constant in TiO2/Al2O3 Nanolaminates Grown on Doped Silicon Substrate by Pulsed Laser Deposition. *Journal of Applied Physics* **2014**, *115* (9). https://doi.org/10.1063/1.4867780.

(18) Ben Elbahri, M.; Kahouli, A.; Mercey, B.; Lebedev, O.; Donner, W.; Lüders, U. Study on the Dielectric Properties of Al2O3/TiO2 Sub-Nanometric Laminates: Effect of the Bottom Electrode and the Total Thickness. *Journal of Physics D: Applied Physics* **2018**, *51* (6). https://doi.org/10.1088/1361-6463/aaa4df.

(19) Padhi, P. S.; Rai, S. K.; Srivastava, H.; Ajimsha, R. S.; Srivastava, A. K.; Misra, P. Maxwell-Wagner Relaxation-Driven High Dielectric Constant in Al2O3/TiO2Nanolaminates Grown by Pulsed Laser Deposition. *ACS Applied Materials and Interfaces* **2022**, *14* (10), 12873–12882. https://doi.org/10.1021/acsami.1c25028.

(20) Padhi, P. S.; Ajimsha, R. S.; Rai, S. K.; Bhartiya, S.; Bose, A.; Das, B.; Tiwari, M. K.; Misra, P. Correlation of Interfacial and Dielectric Characteristics in Atomic Layer Deposited Al2O3/TiO2 Nanolaminates Grown with Different Precursor Purge Times. *Journal of Vacuum Science & Technology A* **2023**, *41* (6). https://doi.org/10.1116/6.0002849.

(21) Padhi, P. S.; Ajimsha, R. S.; Rai, S. K.; Goutam, U. K.; Bose, A.; Bhartiya, S.; Misra, P. Process Temperature-Dependent Interface Quality and Maxwell-Wagner Interfacial Polarization in Atomic Layer Deposited Al2O3/TiO2 Nanolaminates for Energy Storage Applications. *Nanoscale* **2023**, *15* (18), 8337–8355. https://doi.org/10.1039/d3nr00909b.

(22) Sinclair, D. C.; Adams, T. B.; Morrison, F. D.; West, A. R. CaCu3Ti4O12: One-Step Internal Barrier Layer Capacitor. *Applied Physics Letters* **2002**, *80* (12), 2153–2155. https://doi.org/10.1063/1.1463211.

(23) Schmidt, R.; Stennett, M. C.; Hyatt, N. C.; Pokorny, J.; Prado-Gonjal, J.; Li, M.; Sinclair, D. C. Effects of Sintering Temperature on the Internal Barrier Layer Capacitor (IBLC) Structure in CaCu3Ti4O12 (CCTO) Ceramics. *Journal of the European Ceramic Society* **2012**, *32* (12), 3313–3323. https://doi.org/10.1016/j.jeurceramsoc.2012.03.040.

(24) Upadhyay, M.; Ben Elbahri, M.; Mezhoud, M.; Coq Germanicus, R.; Lüders, U. Thickness Dependence of Dielectric Properties in Sub-Nanometric Al2O3/ZnO Laminates. *Solid-State Electronics* **2021**, *186*. https://doi.org/10.1016/j.sse.2021.108070.

(25) Li, J.; Bi, X. Temperature- and Frequency-Dependent Dielectric Behaviors of Insulator/Semiconductor (Al2O3/ZnO) Nanolaminates with Various ZnO Thicknesses. *Journal of Physics D: Applied Physics* **2016**, *49* (28). https://doi.org/10.1088/0022-3727/49/28/285301.

(26) Li, J.; Liu, M.; Bi, X. Interface Electron Polarization Based High-k Al2O3/ZnO Nanolaminates with Excellent Temperature Stability and Ultrahigh Energy-Storage Density by Atomic Layer Deposition. *Journal of Materials Chemistry A* **2019**, *7* (17), 10303–10318. https://doi.org/10.1039/c9ta01487j.

(27) Zhang, Q.; Li, J.; Bi, X. Semiconducting ZnO Effect on Maxwell-Wagner Relaxation in HfO2/ZnO Nanolaminates Fabricated by Atomic Layer Deposition. *Journal of Physics D: Applied Physics* **2014**, *47* (50). https://doi.org/10.1088/0022-3727/47/50/505302.

(28) Van Spronsen, M. A.; Frenken, J. W. M.; Groot, I. M. N. Observing the Oxidation of Platinum. *Nat Commun* **2017**, *8* (1), 429. https://doi.org/10.1038/s41467-017-00643-z.

(29) Fantauzzi, D.; Krick Calderón, S.; Mueller, J. E.; Grabau, M.; Papp, C.; Steinrück, H.-P.; Senftle, T. P.; van Duin, A. C. T.; Jacob, T. Growth of Stable Surface Oxides on Pt(111) at Near-Ambient Pressures. *Angewandte Chemie International Edition* **2017**, *56* (10), 2594–2598. https://doi.org/10.1002/anie.201609317.

(30) Lei, Y.; Jelic, J.; Nitsche, L. C.; Meyer, R.; Miller, J. Effect of Particle Size and Adsorbates on the L3, L2 and L1 X-Ray Absorption Near Edge Structure of Supported Pt Nanoparticles. *Top Catal* **2011**, *54* (5–7), 334–348. https://doi.org/10.1007/s11244-

011-9662-5.

(31) Bergeret, G.; Gallezot, P. Particle Size and Dispersion Measurements. In *Handbook of Heterogeneous Catalysis*; Ertl, G., Knözinger, H., Schüth, F., Weitkamp, J., Eds.; Wiley, 2008; pp 738–765. https://doi.org/10.1002/9783527610044.hetcat0038.

(32) Yoon, S. M.; Seong, N. J.; Choi, K.; Seo, G. H.; Shin, W. C. Effects of Deposition Temperature on the Device Characteristics of Oxide Thin-Film Transistors Using In-Ga-Zn-O Active Channels Prepared by Atomic-Layer Deposition. *ACS Applied Materials and Interfaces* **2017**, *9* (27), 22676–22684. https://doi.org/10.1021/acsami.7b04637.

(33) Chang, M. L.; Wang, L. C.; Lin, H. C.; Chen, M. J.; Lin, K. M. Investigation of Defects in Ultra-Thin Al 2 O 3 Films Deposited on Pure Copper by the Atomic Layer Deposition Technique. *Applied Surface Science* **2015**, *359*, 533–542. https://doi.org/10.1016/j.apsusc.2015.10.144.

(34) Cottre, T.; Fingerle, M.; Kranz, M.; Mayer, T.; Kaiser, B.; Jaegermann, W. Interaction of Water with Atomic Layer Deposited Titanium Dioxide on P-Si Photocathode: Modeling of Photoelectrochemical Interfaces in Ultrahigh Vacuum with Cryo-Photoelectron Spectroscopy. *Advanced Materials Interfaces* **2021**, *8* (11). https://doi.org/10.1002/admi.202002257.

(35) Saari, J.; Ali-Löytty, H.; Kauppinen, M. M.; Hannula, M.; Khan, R.; Lahtonen, K.; Palmolahti, L.; Tukiainen, A.; Grönbeck, H.; Tkachenko, N. V.; Valden, M. Tunable Ti3+-Mediated Charge Carrier Dynamics of Atomic Layer Deposition-Grown Amorphous TiO2. *Journal of Physical Chemistry C* **2022**, *126* (9), 4542–4554. https://doi.org/10.1021/acs.jpcc.1c10919.

(36) Hao, X. A Review on the Dielectric Materials for High Energy-Storage Application. *Journal of Advanced Dielectrics* **2013**, *03* (01), 1330001. https://doi.org/10.1142/s2010135x13300016.

(37) Wittreich, G.; Liu, S.; Dauenhauer, P.; Vlachos, D. Catalytic Resonance of Ammonia Synthesis by Dynamic Ruthenium Crystal Strain. *ChemRxiv* **2021**. https://doi.org/10.33774/chemrxiv-2021-b8kgr.

(38) Ardagh, M. A.; Birol, T.; Zhang, Q.; Abdelrahman, O. A.; Dauenhauer, P. J. Catalytic Resonance Theory: SuperVolcanoes, Catalytic Molecular Pumps, and Oscillatory Steady State. *Catalysis Science and Technology* **2019**, *9* (18), 5058–5076. https://doi.org/10.1039/c9cy01543d.

(39) Gathmann, S. R.; Ardagh, M. A.; Dauenhauer, P. J. Catalytic Resonance Theory: Negative Dynamic Surfaces for Programmable Catalysts. *Chem Catalysis* **2022**. https://doi.org/10.1016/j.checat.2021.12.006.

(40) Dauenhauer, P. J.; Ardagh, M. A.; Shetty, M.; Kuznetsov, A.; Zhang, Q.; Christopher, P.; Vlachos, D. G.; Abdelrahman, O. A. Catalytic Resonance Theory: Parallel Reaction Pathway Control. *Chemical Science* **2020**, *11* (13), 3501–3510. https://doi.org/10.1039/c9sc06140a.

(41) Ravel, B.; Newville, M. *ATHENA* , *ARTEMIS* , *HEPHAESTUS* : Data Analysis for X-Ray Absorption Spectroscopy Using *IFEFFIT*. *J Synchrotron Rad* **2005**, *12* (4), 537–541. https://doi.org/10.1107/S0909049505012719.